Absolute multilateration-based coordinate measurement system using retroreflecting glass spheres

Joffray Guillory, Daniel Truong, Jean-Pierre Wallerand, Christophe Alexandre

Absolute multilateration-based coordinate measurement system using retroreflecting glass spheres

J. Guillory[1], D. Truong[1], J.-P. Wallerand[1], C. Alexandre[2]

1: *Conservatoire National des Arts et Métiers (Cnam),*
Laboratoire commun de métrologie LNE-Cnam,
1 rue Gaston Boissier, 75015 Paris, France.

2: *Conservatoire National des Arts et Métiers (Cnam),*
Centre d'Etudes et De Recherche en Informatique et Communications (CEDRIC),
292 rue Saint-Martin, 75003 Paris, France.

email: joffray.guillory@cnam.fr

Abstract

We have measured the three-dimensional coordinates of retroreflecting glass spheres using a multilateration technique. To this end, the distances between each target and our measurement heads have been determined by an in-house prototype of electro-optical absolute distance meter. The used targets are spheres of glass refractive index n=2 and of diameter 14.2 mm. They offer a much larger aperture than corner cubes and a lower cost, but they present a low reflectivity. However, this paper shows that with a proper collimation of the laser beams it is possible to reach a range of operation of 20 m. The standard uncertainty on such distances is better than 11 µm, including the mechanical errors of the gimbal mechanisms of our aiming systems. This uncertainty has been validated thanks to a comparison with an interferometric bench. In addition, the measurement of the coordinates of 16 glass spheres using a self-calibration multilateration algorithm has also confirmed the performances of the developed system: the standard deviation on the position errors has been estimated to about 10 µm.

Keywords: Large Volume Metrology; Absolute Distance Metre; retroreflecting glass spheres; coordinate measurement system; multilateration technique with self-calibration.

1. Introduction

Many high-value industries are seeking ways to improve their production process. To this end, the industrial robots can increase automation of tasks such as milling, drilling and assembling, and so decrease both operating time and costs. However, the positioning accuracy of these robots are often worse than 0.4 mm [1], which has to be compared to the accuracy of 0.01 mm of a typical machine tool. The robots need therefore to be assisted by external instruments to correct their motion and improve their absolute positioning. Such an approach has been demonstrated for instance in [1, 2] using laser trackers for real-time correction. Industry also uses coordinate measuring systems (CMS) for the alignment of large structures, for instance in the aerospace field where the assembly tolerances of aircraft wings are lower than 0.3 mm [3]. The science facilities request alignments at micrometre levels in a range of tens of meters, for instance to improve the performances of particle accelerators [4], nuclear fusion reactors [5] or large telescopes [6]. Another example of application is the determination of the geometric reference points of astrometric very-long-baseline interferometry (VLBI) space-geodetic systems. From the observation of trajectories of targets mounted on a radio telescope, the telescope can be characterized to determine its invariant reference point, the offset between its axes, and then expressed in an Earth fixed global geodetic reference frame. In this case, a positioning accuracy better than 1 mm is required [7] and recent results already demonstrated uncertainties lower than 50 µm [8].
In practice, the laser trackers are the leading CMS for high-accuracy position measurements. They record a distance along with two angles to provide the target position in a spherical coordinate system. Manufacturer claims for interferometric laser trackers accuracy of 10 µm + 5 µm/m [9], value corresponding to the maximum permissible error (MPE) and mainly limited by uncertainties in the measured angles [10, 11]. However, the positioning errors can be higher in environments without temperature control, for instance in factory workshops. First, the temperature gradients induce beam deflections that impact the measured angles and so the measured positions, up to several tens of micrometres as explained in [12, 13]. Then, in extreme cases as outdoors, the air turbulences compromise the proper functioning of the interferometers.
To overcome these limitations, a multilateration technique based on absolute distance meters (ADM) can be adopted. Multilateration determines the position of a target in space from multiple distance measurements between the target and several separated stations (also named heads) of known coordinates. In that case, only distance information is required. Moreover, the positions of the heads can be determined by a self-calibration process, without additional instruments [14]. We have developed such a system composed of a common ADM and four measurement heads. A previous work has already demonstrated an uncertainty of 4.7 µm on the distance measurements (for a coverage factor k equal to 1) and a range of operation of 140 m, using a hollow corner cube as retroreflector. The three-dimensional coordinates of corner

cubes have also been determined using a multilateration algorithm with self-calibration: the position errors have been estimated at 24 µm in the worst case with a standard deviation around 13 µm in a large volume with distances up to 11.5 m [15].
The hollow corner cubes are well adapted targets for long distance applications with very low optical losses. However, they have a limited acceptance angle of, in the best case, 60°. They must therefore be aligned in the direction of the measurement head. In practice, the corner cube is mounted on a motorized gimbal mechanism which can be remotely controlled. This brings complexity, and adds measurement errors. Indeed, if the centre of the corner cube is not perfectly positioned at the intersection of the two rotating axes of the gimbal mechanism, or if the gimbal mechanism presents some misalignments, the measured distances vary with the orientation of the target. As demonstrated in [15], the uncertainty contribution of such a mechanical design to a distance measurement can be reduced to 3.9 µm, which remains the main contribution of the multilateration system we have developed.
The cat's eye retroreflector, an alternative to the corner cubes widely used for laser interferometer systems, can also be used for the multilateration systems. They offer a larger acceptance angle, up to 150° [16]. However, to be visible from almost any angle, the use of a gimbal mechanism for the target is still necessary.
The use of a retroreflecting sphere of n=2 as retroreflector, originally an idea of Takatsuji [17], enables an acceptance angle as large as 360° in principle. Thus, the target can be seen from any angle, and so visible from several measurement heads simultaneously, which could make possible real time multilateration. In addition, as it does not require gimbal mechanism, it is more compact, simpler to use, and does not induce mechanical source of error.
The purpose of this paper is to validate the multilateration system we have developed using glass spheres of refractive index n=2 as retroreflector instead of hollow corner cubes. We aim at a range of operation of at least 10 m like in [18] where absolute distance measurements were performed with a laser tracker based on pulsed interferometry, or like in [19] where the distance measurements were performed with a frequency scanning interferometer. In our case, it will be shown that such a range is reached and that distances up to 20 m can even be considered with some optimisations, which can address a wide range of applications.
The work described in this paper is organized as follows. In the next section the multilateration system is presented. Section 3 explains the principle of the reflection on a glass sphere using a ray-tracing simulation. Then section 4 evaluates experimentally the performances of this target in terms of received power, the most important criteria to perform accurate distance measurements. It will be emphasized that there is an optimal beam collimation for propagation over long distances. Section 5 evaluates the uncertainty of our absolute distance measurement system when it is used with such a glass sphere. Lastly, section 6 evaluates experimentally the performances of the multilateration system with self-calibration technique and 16 positions of the glass sphere to be determined in a small volume.

2. The multilateration system

As depicted in Fig. 1, the multilateration system consists of three parts: a common ADM, four measurement heads named A, B, C and D, and one (or several) target.

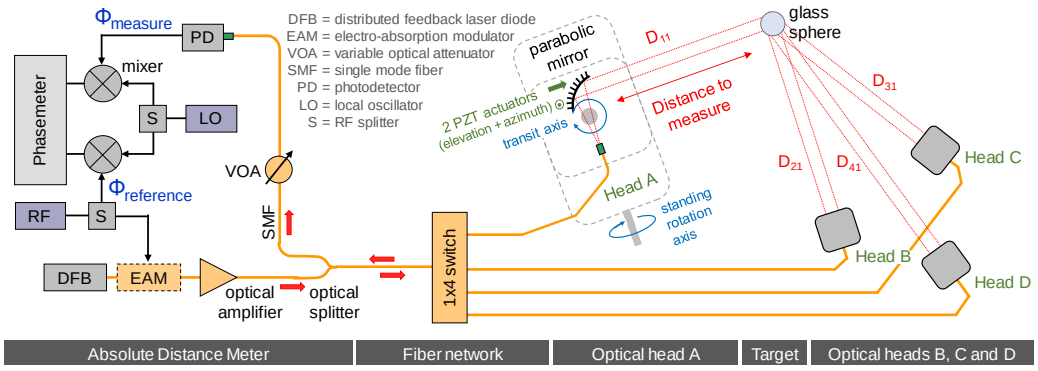

Fig. 1. Functional diagram of the multilateration system.

2.1. The absolute distance meter

The ADM determines the distances $d_{i,j}$ between each measurement head i and a target position j. To do this, a phasemeter measures the phase accumulated by a Radio Frequency (RF) carrier, which is propagated in air by a laser beam at 1550 nm:

$$d = \frac{1}{2} \times \left(\frac{\phi}{2\pi} + k \right) \times \frac{c}{n \times f_{RF}} \quad (1)$$

where ϕ is the measured phase shift, c the speed of light in vacuum, n the group refractive index of air, f_{RF} the frequency modulation, and k an integer number corresponding to the number of synthetic wavelengths $\Lambda = c / (n \times f_{RF})$ within the

distance to be measured. In practice, the RF signal is processed by a Field Programmable Gate Arrays (FPGA) where each individual phase measurement is integrated over 20 ms.
The developed ADM uses affordable components from the telecommunications world. At the emitter side, the modulated signal comes from a Distributed FeedBack laser diode (DFB) modulated at 4895 MHz by an Electro-Absorption Modulator (EAM), while at the receiver side, the phase-shifted signal is detected by a PIN photodiode. Before this photodetection, a variable optical attenuator has been implemented to always get a suitable RF power at the phasemeter input. The choice of a fiber-guided ADM enables to use a common system between several spatially separated heads connected all together thanks to an optical-fiber network and an 1x4 optical switch.

2.2. The measurement heads

The measurement heads play the role of collimating system and of aiming system. To achieve these points, and as detailed in Fig. 1 for head A, a 90° off-axis parabolic mirror has been set up to collimate the optical beam coming from the ADM. It is mounted on a two-stage gimbal mechanism for rotation of the laser beam in every direction of space and around an invariant point in space.
The first stage of the gimbal mechanism consists of a movable platform rotating around two perpendicular axes (standing and transit axes), which can be oriented in any direction with an angular resolution of around 450 µrad using stepper motors. This stage is used for the coarse alignment of the beam on the target.
For a fine alignment, and as shown in Fig. 2, the parabolic mirror has been mounted on a second gimbal mechanism driven by two linear piezoceramic actuators. This second stage offers an angular motion around 2 mrad with a resolution better than 1 µrad. However, the angular displacement of the collimating mirror impacts the beam collimation. This point is studied in section 4.

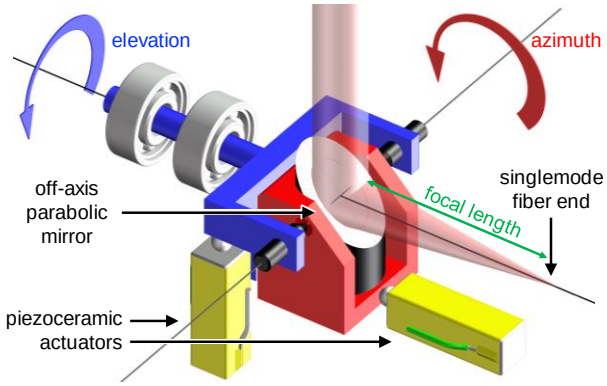

Fig. 2. The second stage of the gimbal mechanism.

This two-stage gimbal mechanism is an unusual approach compared, for instance, to the ones adopted by the commercial total stations, which are based on linear piezoceramic actuators acting laterally on a ring-shaped runner to create the rotary motion. However, even if our approach does not allow continuous motion with high speed, it offers an affordable aiming system of high angular resolution. In the current system, the aiming process is manual. The measurement heads cannot track a moving target, they can only rotate to recorded angular positions thanks to encoders or perform a slow angular scan around an angular position until they detect a signal.
At the end, each measurement head is subject to misalignments, offsets and eccentricities that lead to errors on the distance measurements: this has been studied in [15] and their global standard uncertainty contribution to a distance measurement is equal to 1.4 µm (k=1).

2.3. The glass sphere target

The design of the target is depicted in Fig. 3. It is a sphere of 14.2 mm diameter made of TAFD65 glass from Hoya Corp. with an index n very close to 2 (n = 1.99890 at λ = 1529.6 nm [20]). This sphere rests on three feet on the top of the holder. The latter, highlighted in red in Fig. 3, are portions of a 90° solid cone. The contact between the sphere and these feet is therefore a portion of a circle. The in-house fastening system to prevent the glass sphere from falling down is based on a harness with three arms of 0.30 mm wide and 0.12 mm thick. Two of these arms are fixed to the holder by simple screws, while the third arm is fixed by a spring. By this way, a moderate force is always applied on the glass sphere whatever the temperature. However, the fastening system has some drawbacks: the stainless-steel harness may scratch the surface of the glass, and the optical beam can be partly masked by the harness. This last point will be studied in section 5.3. At the end, the developed design offers a zenithal aperture of 240° and azimuthal aperture of 360°.

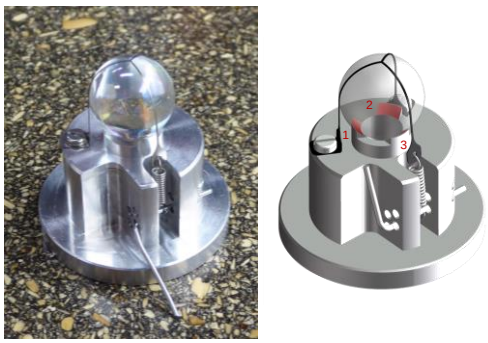

Fig. 3. The retroreflecting sphere and its in-house fastening system. On the left, a photograph of the developed target, and on the right, the 3D model with the feet of the holder in red.

Other holding options to maintain the glass sphere on its holder could be considered such as vacuum suction or glue. Keeping vacuum in a chamber underneath the glass sphere is difficult without pumping regularly. Moreover, this option requests a seal between the sphere and the holder. Gluing is an appropriate solution if the glue is stable in time with bonds that resist shocks. However, the harness appeared to us as the best option since it is very resistant to shocks and it allows to disassemble the ball from its holder without great damage.

3. Principle of retroreflecting spheres of glass refractive index n=2

Fig. 4 depicts a ray tracing view of the propagation of the laser beam in air up to the target. The optical beam emerges from a singlemode fiber of 0.095 effective numerical aperture, then it is collimated by an off-axis parabolic mirror located at 33 mm from the fiber. Thus, an optical beam of 6.3 mm diameter is obtained. When this beam reaches the target, it crosses the sphere a first time, focuses on its rear face, reflects on the glass-air interface, and crosses back the sphere again. The portion of incident light reflected (R) and transmitted (T) at the boundary between the two mediums is:

$$R = [(n_{glass} - n_{air}) / (n_{glass} + n_{air})]^2 = (1/3)^2 = 11.1\ \% \text{ and } T = 1 - R = 88.9\ \% \qquad (2)$$

Therefore, the glass sphere presents a low reflectivity with an optical signal reduced by 10.6 dB.

$$R_{total} = R \times T^2 = 8.8\ \% \qquad (3)$$

In addition, the incident light is reflected back with an important beam deflection [21, 22], which reduces still further the received power.

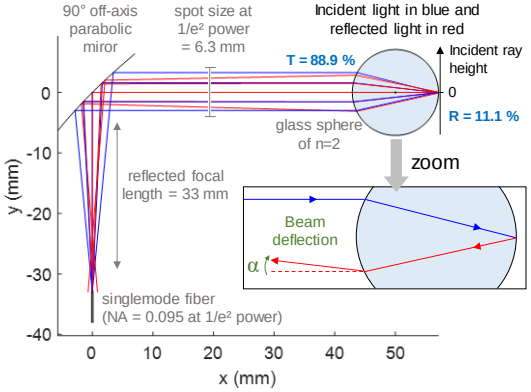

Fig. 4. Propagation of the laser beam up to the target using ray tracing.

This deflection simulated under Matlab using a classical ray tracing approach (and depicted in Fig. 4) depends on two parameters: the glass index and the height of the incident ray. As depicted in Fig. 5, with an index value slightly smaller than 2, there are three different areas where the beam deflection is equal to zero. For these incident ray heights, the reflected beam is parallel to the incident beam and it will be reinjected in the singlemode fiber. On the contrary, if the deflection becomes too high, the reflected beam will not reach the fiber. In our simulations, the criterion to validate the reinjection in the fiber is the position of the optical ray after full propagation: it should be inside the 17.9 µm of the mode field diameter of the singlemode fiber, i.e. twice the distance from the fiber center where the intensity of the output beam has dropped down to 1% of its total intensity (corresponds to 10.4 µm at $1/e^2$). By this way, the full beam is considered. The fraction of the incident gaussian beam reinjected in the singlemode fiber is called the effective reflection area.

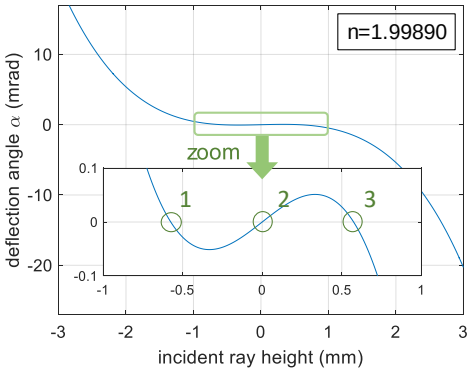

Fig. 5. Deflection angles at the output, i.e. after reflection, of a sphere of diameter 14.2 mm obtained from ray-tracing simulations.

The results of the ray-tracing simulation with a glass sphere positioned at 0.5 m, with the assumption of a gaussian beam perfectly collimated (divergence of the gaussian beam has not been taken into account), show that only the portion of the light corresponding to deflection angles lower than 27 mrad is reinjected in the fiber after propagation in air and reflection on the glass sphere. This induces 4.9 dB of additional optical losses. Cumulated with the 10.6 dB of optical losses due to the reflection of the beam on the glass sphere material, total optical losses of 15.5 dB are obtained. In practice, 18 dB more optical losses (i.e. 36 dB for the RF signal at the input of the phasemetre) have been observed when a glass sphere is used instead of a corner cube for short distances, which is very close to the value of 15.5 dB from the simulations. This will limit the range of operation of our system. However, the collimation of the laser beam can be adjusted to optimize it as will be shown in the next section.

4. Effects of the beam collimation on the received power

The simulations help to understand the mechanisms responsible for the optical losses after reflection on the sphere, but they are not sufficient to finely quantify and so predict the losses observed experimentally. Actually, the beam collimation has to be taken into account for more realistic simulations. Thus, the distance between the fibre end and the parabolic mirror has been set differently on the different measurement heads to study the effect of the beam collimation on the received power and so on the range of operation of the telemetric system.
The results are summarized in Fig. 6. For each head, and different piezoceramic actuator configurations (the ones mounted on the parabolic mirrors to finely aim at the targets), the RF power measured at the phasemeter input was recorded as a function of the distance up to the glass sphere. This shows that the received power for a given distance strongly depends on the collimation of the laser beam, as expected. If similar curves are obtained for the heads A, B and C with a received power which decreases as the distance increases, the head D presents a different behaviour: first, the received power increases, up to about 10 m, then it decreases with an important drop of around 2 dB/m. At the end, the head D receives more RF power up to 22 m, compared to other heads.
Moreover, the behaviour of the heads also depends on the piezoceramic actuators that control the fine alignment, especially for the heads B and D. As a reminder, these actuators can move the collimating mirror if the latter is not well centered on its gimbal mechanism, and thus impact the beam collimation (see Fig. 2).

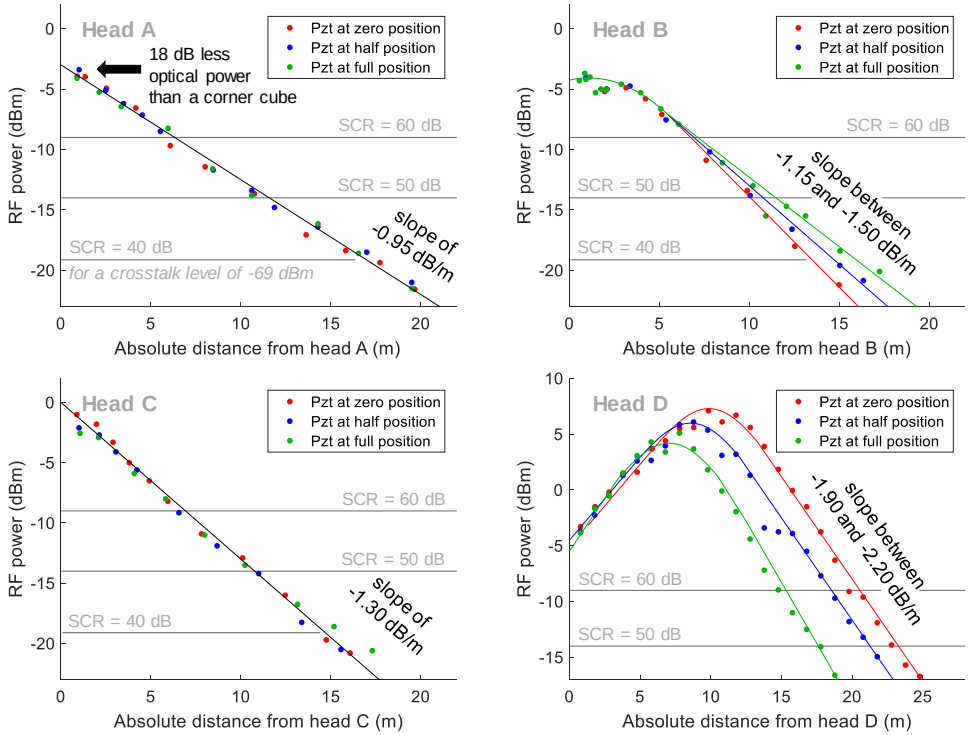

Fig. 6. Received RF power as a function of the distance for different beam shapes. The horizontal lines show the RF power level for which the Signal to Crosstalk Ratio (SCR) takes different values for a crosstalk at -69 dBm.

To quantify the divergence of the different beams, their intensity profile has been recorded along the two orthogonal axes of the parabolic mirrors, X (in the plane of the laser beam) and Y. An example corresponding to the head C, piezoceramic actuators in their zero position, and a distance of 7.7 m is presented in Fig. 7. The diameters of the beams on these axes were then measured for different distances.

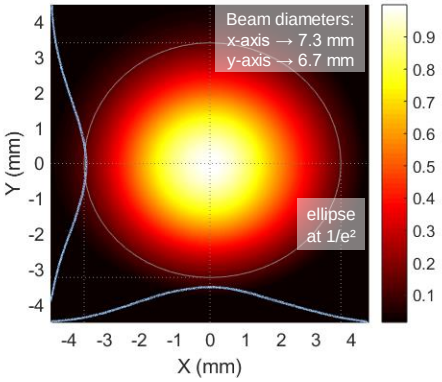

Fig. 7. The intensities of a laser beam along the two main axes of the parabolic mirror and the 2D reconstruction of the beam profile.

The variation of a gaussian beam radius ω with the distance z is given by:

$$\omega(z) = \omega_0 \times \sqrt{1 + \left(\frac{\lambda \times (z + z_0)}{\pi\, {\omega_0}^2}\right)^2} \qquad (4)$$

where z_0 is the position of the beam waist, i.e. where the beam radius reaches a minimum value, ω_0 is the waist, i.e. the minimum radius, and z is the distance travelled by the beam from the parabolic mirror. If the parabolic mirror is positioned at a distance equal to its reflective focal length from the optical fibre end (33 mm in our case), we should obtain a gaussian beam well collimated with a beam waist of 3.1 mm located on the parabolic mirror (z_0=0). The dashed line in Fig. 8 on the left shows how the beam diameter should evolve in such a case: it diverges and at a distance of 20.1 m corresponding to the Rayleigh range, the beam diameter is $\sqrt{2}$ larger than its waist. In this figure, the blue and red points are the beam diameters of the head C measured from the recorded intensity profiles in X and Y axes, respectively, and the corresponding solid lines are the best fitting curves from the mathematical model in formula (4). This reveals the existence of a strong asymmetry between the transverse beam profiles, which are due to the inevitable misalignments of the off-axis parabolic mirror.

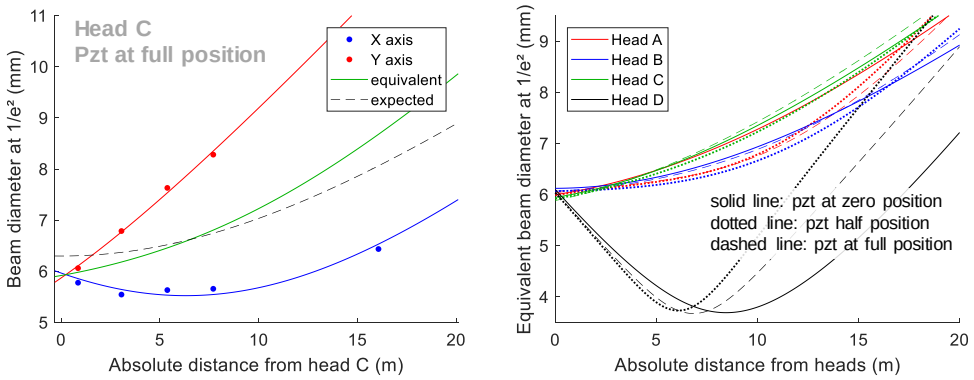

Fig. 8. Beam diameters at 1/e² as a function of the absolute distance from the measurement heads. On the left: beam diameters of the head C on both axes X and Y. On the right: equivalent beam diameters for the four measurement heads and for different positions of their piezoceramic actuators.

To take into account these asymmetries, we have introduced an equivalent beam radius $\omega_{equivalent}$ to characterize the laser beams with a single parameter. This equivalent beam radius is defined as the radius of a virtual circular beam of the same area as the measured beam, assuming that the actual beam has an elliptical profile of area $\pi \times \omega_x \times \omega_y$ with ω_x and ω_y the beam radius measured on the X and Y axes:

$$\omega_{equivalent}(z) = \sqrt{\omega_x(z) \times \omega_y(z)} \tag{5}$$

Fig. 8 on the right presents the equivalent beam diameters of the four heads. Comparing these curves with the ones in Fig. 6, it appears that the equivalent beam width is strongly correlated to the received RF power, as expected since the RF power (in dB) should be proportional to $-20 \cdot \log_{10}(\pi \cdot \omega(z)^2)$.
This demonstrates that the RF power received after reflection on the glass sphere can be optimized by adjusting the beam collimation. To understand why, the parabolic mirror of reflected focal length f = 33 mm has been considered as an ideal thin lens of same focal length. Thus, using the equation developed in [23], the waist of the input beam has been processed as an object and the waist of the output beam as an image. For a gaussian beam, the position of the waists relatively to the parabolic mirror can therefore be described as:

$$\frac{1}{z_0} = \frac{1}{z_s + \frac{{z_R}^2}{(z_s + f)}} + \frac{1}{f} \tag{6}$$

where z_s and z_0 are the waist positions of the input and output beams, respectively, and z_R is the Rayleigh range of the input beam. It is equal to:

$$z_R = \frac{\pi \times {\omega_s}^2}{\lambda} = \frac{\pi \times \left(0.5 \times 10.4 \cdot 10^{-6}\right)^2}{1550 \cdot 10^{-9}} = 54.8\ \mu m \tag{7}$$

with ω_s is the waist of the input beam, in our case it is the mode field diameter of the singlemode fiber at 1/e².
The calculation of z_s as a function of z_0 from formula (6) consists in solving a quadratic equation, which has two solutions. As a consequence, the focal error z_s+f depicted in Fig. 9 on the left has also two possible values. At this point, the ambiguity was resolved choosing the focal error inducing a theoretical output waist the closest to the measured one.
At the end, for all the measurement heads, the focal error decreases on the X axis and increases on the Y axis when the piezoceramic actuators travel from their zero position to their full position, with variations included between 30 µm and 73 µm. This demonstrated that the parabolic mirrors are not well centred on their gimbal mechanism, with always systematic positioning errors in the same direction.
The theoretical output waist ω_0, depicted in Fig. 9 on the right, is then determined by the following equation:

$$\omega_0 = \frac{\omega_s}{\sqrt{\left(1 - \frac{z_s}{f}\right)^2 + \left(\frac{z_R}{f}\right)^2}} \tag{8}$$

The output waist location has both minimum and maximum possible values, which are obtained when the parabolic mirror is shifted of $\pm z_R$ from its nominal value f. When the parabolic mirror is too close to the fiber end, at $z = -z_R$, the output beam focuses at 10 m to reach a minimum radius of 2.2 mm as shown in Fig 9 on the right, then it diverges. This corresponds to the best setting of the parabolic mirror for propagation up to 20 m. Nevertheless, the gain of received

power before 20 m is rapidly lost for longer distances due to high beam divergence and so greatest loss per meter. For long distances, it is better to limit the beam divergence and so respect the focal length of the parabolic mirror.

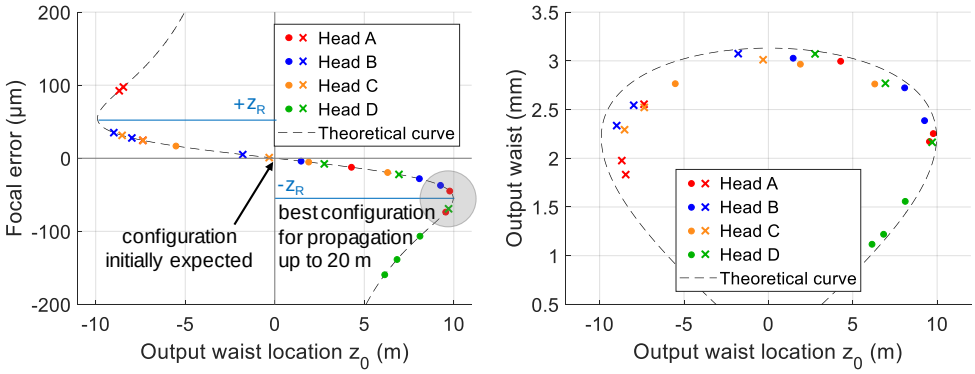

Fig. 9. Focal error and output waist as a function of the output waist location for the two axes, X is depicted with dots while Y is depicted with crosses.

In practice, the beam waist should be located at 10 m from the parabolic mirror (like the measurement head D) to optimize the received optical power up to 20 m.

5. Uncertainty assessment on a distance measurement

The assessment of the uncertainty on a distance measurement is quite complex as it depends on many parameters: the different sources of errors due to the telemetric system, and the ones due to the mechanical designs of the measurement heads and the glass sphere. A last factor is the knowledge of the group refractive index of air, already studied in [15], even if it is not specific to the developed system.

5.1. Sources of errors due to the telemetric system

As shown in formula (1), the calculation of the distance is based on the value of the modulation frequency f_{RF}, known with an uncertainty of 1.5 10^{-9} thanks to a lock on a 10 MHz atomic Rubidium clock, and on the measurement of a phase shift ϕ. The uncertainty on the phase measurement depends on different sources of errors: the crosstalk, the amplitude-to-phase coupling, and the random noise. The contribution of each of these errors has already been studied in [24] when a hollow corner cube is used as target. When a glass spheres of n=2 is used, the magnitude of these contributions is significantly different.
The main difference comes from the effect of the crosstalk, which refers to the addition of a spurious signal at f_{RF} to the ideal measurement signal due to optical and electromagnetic leakages from the emission stages to the reception ones. In practice, the RF level of this spurious signal can be up to -69 dBm. When a glass sphere is used as target instead of a corner cube, the Signal to Crosstalk Ratio (SCR) depends much more on the measured distance. As shown in Fig. 6, the received signal can vary by more than 20 dB over 20 m, which can lead to SCR lower than 40 dB. As explained in [24], such values induce a related uncertainty component varying from 3.4 µm for 60 dB of SCR to 34.5 µm for 40 dB of SCR. In addition, the random noise, which refers to the noise performance of the phasemeter with input signals that have been propagated through the whole system, is higher when a glass sphere is used as a target, keeping a low value of 2.1 µm, compared to 0.8 µm for a corner cube.

Table I. Sources of errors of the telemetric system and their contributions when a glass sphere is used.

Parameter		Description	Value	Contribution (k=1)	Error distribution
1	u_{RF}	modulation frequency	f_{RF} = 4895 MHz	$1.5 \cdot 10^{-9} \times L$	gaussian distribution
2	$u_{crosstalk}$	crosstalk	SCR from 60 dB to 40 dB	3.4 µm to 34.5 µm	arcsine distribution
3	$u_{AM/PM}$	amplitude-to-phase coupling	5 dB power variations	0.2 µm	uniform distribution
4	u_{noise}	random noise	σ_φ = 0.43 mrad	2.1 µm	gaussian distribution

To determine the impact of the four additive sources of errors in Table I on a distance measurement, a Monte Carlo simulation has been performed as described in [15]. At the end, the uncertainty contribution of the telemetric system equals to 4.0 µm (k=1) for a SCR of 60 dB. However, it can increase to 11.1 µm for a SCR of 50 dB, which corresponds to propagation distances up to 20 m when the beam collimation is optimized, such as head D. For the other heads, a SCR of 50 dB corresponds to a typical distance of 10 m (Fig. 6).

5.2. Sources of errors due to the mechanical designs.

Like any mechanical system, the gimbal mechanisms developed for the measurement heads are not perfectly machined and assembled. This induces errors on the geometric distances, which depend on the angular orientations of the heads. The latter, shared by other instruments such as the laser trackers, total stations or theodolites, and well described in literature [25], have been studied for our specific design [26] considering only the errors that affect the measured distances (not the angles), i.e. the relevant errors for a multilateration system. It was concluded that the mechanical errors of the measurement heads are characterized by a Lorentzian distribution with a standard deviation of only 1.4 µm.
Besides, the mechanical errors induced by the glass sphere roundness are even smaller. According to the manufacturer, the balls are produced with a roundness value (RONt), i.e. difference between the maximum and minimum radial deviation from the least square reference sphere, of around 0.3 µm, which corresponds to a standard uncertainty contribution of 87 nm assuming uniform distribution (k=1) and which is negligible compared to other contributions. Lastly, the average value of the sphere diameter is known with an uncertainty of 5 µm (k=1). But this systematic error is included in the offset instrument, which is determined automatically thanks to multilateration algorithm with self-calibration.

5.3. Effect of the harness.

To quantify the interaction between the optical beam and the harness that maintains the glass sphere, the target has been placed at the centre of two rotation stages (one horizontal and one vertical), at a distance of 1.15 m from the measurement head A. Thus, as depicted in Fig. 10, the RF power received by the phasemeter has been recorded for different angle positions of the glass sphere, with or without interaction of the optical beam with the harness or the feet which carries the sphere.
First, by tuning the azimuthal angle, three different situations have been characterized: when the incident beam crosses one of the arms of the harness at the rear face of the sphere, i.e. at its focus point (1st case), when it hits one of the arms at the front face of the sphere (2nd case), and lastly when it avoids any contact with one of the arms (3rd case). In the 1st case, due to reflection on the metallic surface of the harness, an increase of the RF power up to +15 dB is observed. This interaction between the optical beam and the harness occurs only for very precise angles, over ~0.5°. Then, in the 2nd case, when the incident beam crosses one of the arms of the harness at the input of the sphere, around 10 dB of additional optical losses are observed. In Fig. 11, a photograph on the left depicts this case, and curves on the right show the variations of the received RF power in detail for angles between 311° and 332°. The simulated and experimental curves are very similar, even quantitatively, although the ray-tracing simulation in a two-dimensional plane is a limited approach.
As explained previously, only a fraction of the incident gaussian beam is reinjected in the singlemode fiber due to beam deflection. This fraction, called effective reflection area, is depicted in brown in Fig. 12, case a). This area varies when one arm of the harness obstructs a part of the incident beam: the part that hits the arm at the input of the sphere, represented in red, and the one that hits the arm after reflection on the rear surface of the sphere, represented in blue, are two areas of the beam which are masked, symmetrically with the central axis of the beam. In case b), this only impacts the ends of effective surface area. The received power begins to decrease. In case c), as the arm has moved with the rotation of the stage, parts of higher power of the beam of gaussian profile are then masked. The received power continues to decrease. At one point, in case d), the two parts begin to overlap: the closer the arm approaches the centre of the beam, the more the masked surface of the beam decreases. The received power increase and we observe in case e) a local peak of received power.
The RF power received by the phasemeter has also been recorded as a function of the elevation angle for an azimuth angle fixed to 261.5°, i.e. when the optical beam interacts with the harness over a wide range or with one of the three feet which carry the sphere. In this case, the elevation angle can vary between 65° et 310°, i.e. an aperture of 245°. As previously, the reflection on the metallic harness increases the received power with gains up to +15dB. Around 151°, there is also a strong interaction between the optical beam and one of the three feet on which the sphere is installed.

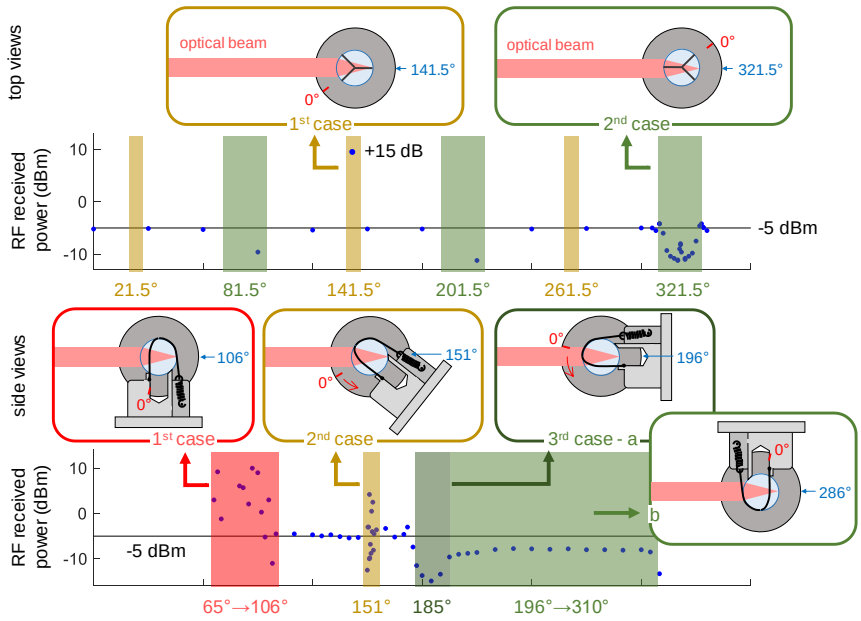

Fig. 10. Impact of the harness: received power when the sphere is rotated around its vertical axis (at the top) and its horizontal axis (at the bottom).

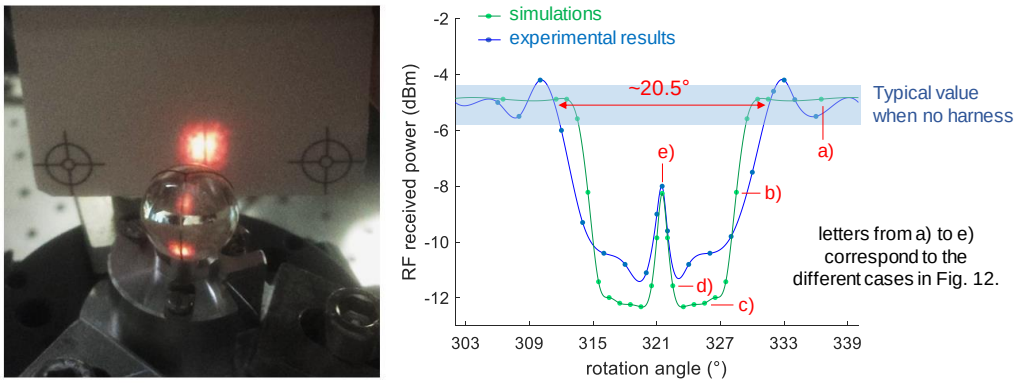

Fig. 11. Photograph of the harness when one of its arm passes in front of the incident beam on the left and the corresponding RF power variations observed and simulated on the right.

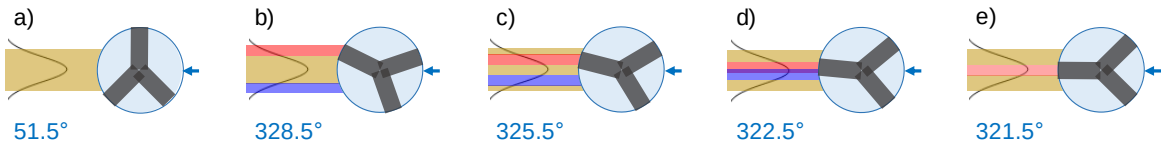

Fig. 12. Impact of the harness when one of its arm passes in front of the incident beam coming from the left: effective reflection area in brown, and parts of the incident and reflected beam masked by the arm in red and blue, respectively.

For the different points in Fig. 10, the distance up to the sphere has also been measured as a function of the angle of the rotation stages. The harness has no specific impact on the measured distances in terms of absolute value or random noise, except when the RF losses are too significant, i.e. typically higher than 10 dB. In that case, the SCR value predicts well the uncertainty on the measured distance.

We could expect that when the optical beam is partially reflected by the surface of the harness, and when the harness is not perfectly in contact with the sphere, errors in the distance measurement would be observed. In practice, such a case has not been identified. This can be explained by the fact that, when the harness is not in contact with the sphere, a small angle between them avoids the reflection of the optical beam on the harness to be reinjected into the fiber.

5.4 Global uncertainty on a distance measurement

Previous parts have shown there is two additive sources of errors. The main uncertainty contribution comes from the telemetric system, which mainly depends on the SCR and so on the received power. It has been estimated to 4.0 µm (k=1) for a SCR of 60 dB, and of 11.1 µm for a SCR of 50 dB. The second uncertainty contribution comes from misalignments in the two-stage gimbal mechanism of each measurement head. It has been estimated to 1.4 µm (k=1). At the end, these

two sources of errors lead to a combine uncertainty on a distance measurement equal to 4.3 µm (k=1) for a SCR of 60 dB, and of 11.2 µm for a SCR of 50 dB.

5.5 Comparison with an interferometric bench.

a) Hollow corner cube as target

The validation of the uncertainty budget of the telemetric system is achieved by a comparison with a laser interferometer. As depicted in Fig. 13, this has been done for length displacement up to 35 m: the ADM beam, propagated over 35 m, has been corrected by the group refractive index of air for a wavelength at 1550 nm, while the interferometric beam propagated over 70 m thanks to double roundtrip has been corrected by a factor of 2 and by the phase refractive index for a wavelength at 633 nm.

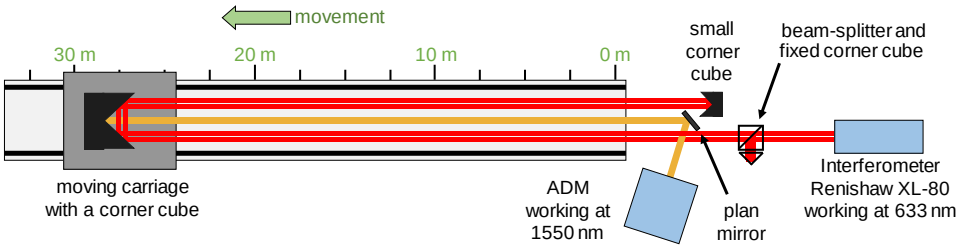

Fig. 13. Comparison between an interferometer and the ADM using a corner cube as target.

To get the best possible conditions in terms of received power, and so minimize the crosstalk effect, the comparison has been first performed with a hollow corner cube as target. This provides a reference measurement. In such a case, the received power can be adjusted thanks to a variable optical attenuator before the photodetection to get, for all the measured distances, a RF power around -4 dBm and a SCR higher than 65 dB.
The difference between the interferometric distance and the ADM distance is presented in Fig. 14. It is characterized by a standard deviation of 2.2 µm. Small displacements over two synthetic wavelengths around 1.8 m and 26.8 m demonstrates the absence of cyclic error (crosstalk better than 65 dB).

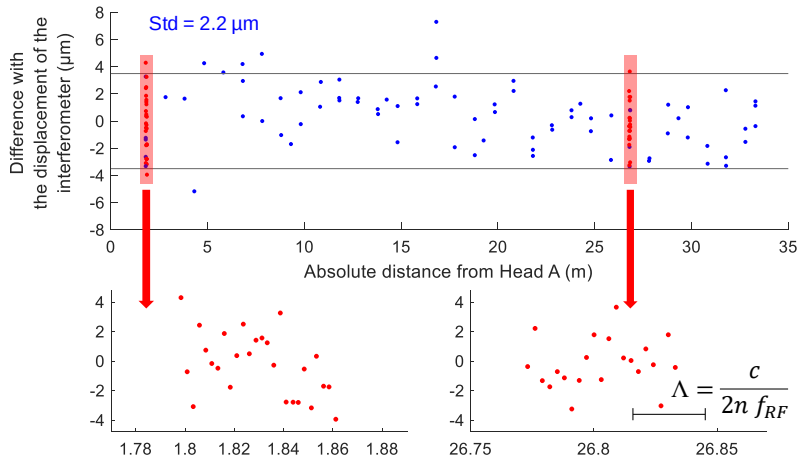

Fig. 14. Difference between the interferometer and the ADM with a corner cube as target.

b) Retroreflecting sphere of n=2 as target

In a second time, the ADM has been compared to the laser interferometer using the retroreflecting sphere of n=2. In this new setup depicted in Fig. 15, the corner cube mounted on the moving carriage is used in a direct way for the interferometric measurement, while the glass sphere is reached by our ADM after reflection on this corner cube. In practice, the movement of the carriage around the measurement axis (because the bench is not perfectly aligned) adds locally important drops of the received RF power, which limits the characterization of our system. To fix this problem, i.e. to always reach the maximum possible power and so to minimize the crosstalk effect, a piezoelectric mirror has been added at the ADM output to refine the alignment on the retroreflecting sphere. However, these angle corrections are small enough to have a negligible impact on the measured distances.

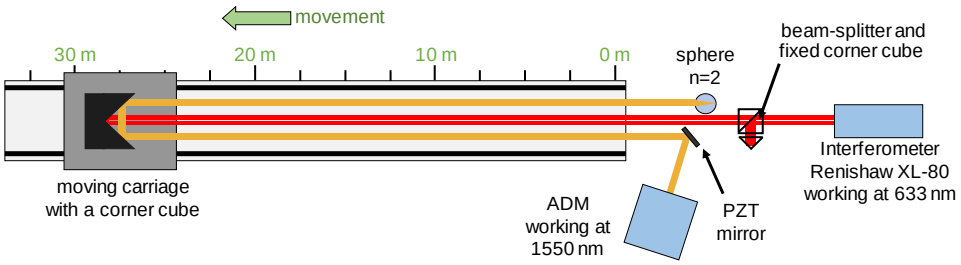

Fig. 15. Comparison between an interferometer and the ADM using a sphere of n=2 as target.

At the end, the different reflections on the mirrors, i.e. the piezoelectric mirror (silver mirror with ~96% of reflectance at 1.5 µm) and the three faces of the corner cube (aluminium mirrors with ~92% of reflectance at 1.5 µm), induce for this double roundtrip 5 dB additional RF losses (L_{RF}).

$$L_{RF} = 20\log_{10}(0.96^{1\times2} \times 0.92^{3\times2}) = \text{-}5.1 \text{ dB} \quad (9)$$

The comparison has been achieved using the measurement head D with its piezoceramic actuators in their zero position to optimize the received power up to 20 m. The RF power as a function of the distance follows the same curve as the one presented in Fig. 6 (the red curve of the head D) with just 5 dB additional losses. During this comparison, the crosstalk level was close to -81 dBm and the SCR was higher than 60 dB up to 23 m. At such a value, and as explained in section 5.1, the uncertainty contribution of the telemetric system should be equal to 4.0 µm (k=1). The results, presented in Fig. 16 in blue, are consistent with the expectations: the difference between the interferometric distance and the ADM one is lower than 8 µm up to 22 m with a standard deviation of 3.3 µm. These results validate the uncertainty budget defined in Table I.

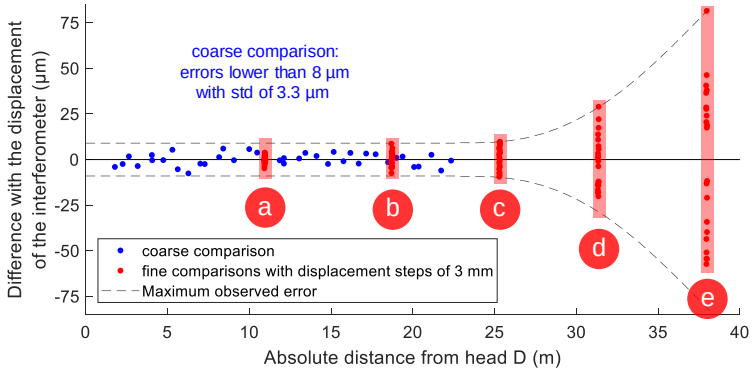

Fig. 16. Difference between the interferometer and the ADM with the glass sphere as target and when the measurement head D is used.

Displacements over two synthetic wavelengths with small steps of 3 mm have also been done at different distances (indicated by letters from a to e in Fig. 16) to reveal the presence of the cyclic error. Magnification of these curves are presented in Fig. 17. At the end, the cyclic error is written as follow:

$$cyclic\ error\ = a \times sin\left(2\pi \frac{d}{\Lambda} + \varphi_0\right) \text{ with } \Lambda \sim 30.6\, mm \quad (10)$$

In Fig. 17, the parameters a and φ_0 of the cyclic errors have been determined by the least squares method. The amplitude of this cyclic error, i.e. the factor a, is directly related to the SCR:

$$a = \frac{1}{4\pi} \times \frac{c}{n \times f_{RF}} \times 10^{-SCR/20} \quad (11)$$

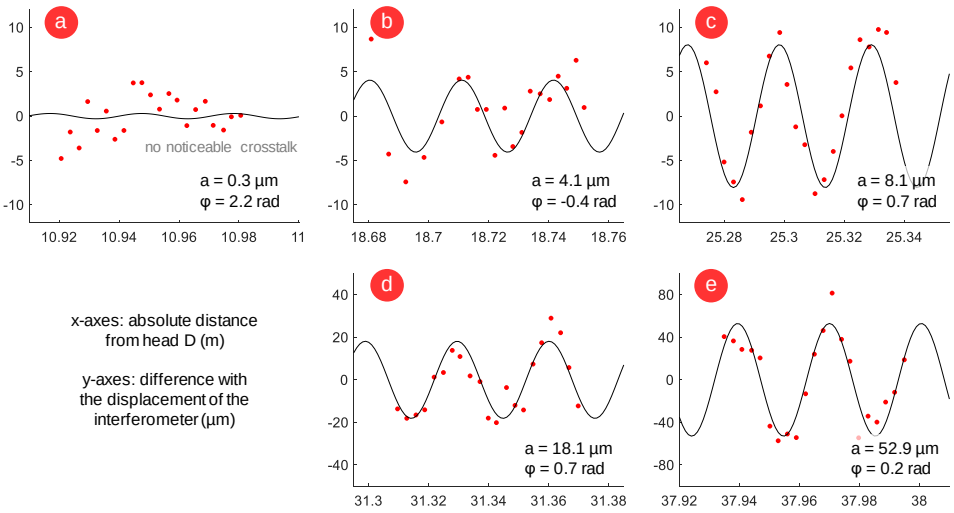

Fig. 17. Difference between the interferometer and the ADM for small displacements.

For each curve in Fig. 17, the SCR is measured, and so an expected amplitude of periodic error, has been calculated. This is detailed in Table II: the cyclic error experimentally obtained is very close to the expected one.

Table II. Analysis of the crosstalk.

case	received RF power (dBm)	distance associated to this RF power if no mirror losses (m)	SCR for a crosstalk at -81 dBm (dB)	expected error amplitude (µm)
a	-4.3	18.0	76.7	0.7
b	-10.9	21.6	70.1	1.5
c	-23.4	28.4	57.6	6.4
d	-33.2		47.8	19.8
e	-41.3		39.7	50.4

At the end, the main limitation is the crosstalk, which depends on the received power and on the crosstalk level. Without the 5dB of additional losses due to the different reflections on the mirrors, the received power can be deduced from Fig. 6. As for the crosstalk level, it varies over time between -81 dBm and -69 dBm.
On the assumption of the worst case, i.e. a crosstalk level at -69 dB, the power received by the measurement head D is sufficient up to 23 m to obtain a SCR higher than 50 dB and so a cyclic amplitude error lower than 15.4 µm when comparing with an interferometer: as explained in section 5.1, this induces an uncertainty contribution equals to 11.1 µm (k=1) considering all the sources of error of the telemetric system. The other measurement heads, with a beam collimation complying with the value of the focal length of the parabolic mirror, can claim similar performances for distances up to ~10 m only.

6. Experimental validation by a multilateration coordinate measurement

This part evaluates experimentally the performances of the developed system through position measurements based on a multilateration technique when it is used with a retroreflecting sphere of glass refractive index n=2. This is a way to verify the accuracy of the whole system, by taking into account the uncertainties on each distance measurement established in section 5, but also the uncertainty induced by the multilateration algorithm with self-calibration. The latter is not detailed here, as it would require a dedicated study in a separate paper.

6.1. Configuration

The four measurement heads have been connected to the telemetric system by 2m-long singlemode fibres for the heads A, B and C, and a 10m-long fibre for the head D. As shown in Fig. 18 and 19, they form a tetrahedron with edges between 1.1 m and 1.6 m. Their coordinates are:

A = [0, 0, 0], B = [547, -194, 967], C = [1100, 0, 0] and D = [555, 1318, 537] (units in mm).

This is close to a regular tetrahedron, one of the optimal configurations for multilateration algorithm as explained in [27]. Then, 16 different target positions have been chosen: 14 points are inside the volume formed by the 4 measurement heads, and 2 points have been positioned largely outside for testing longer distances, up to 3.5 m. In this configuration, the smallest measured distance is equal to 226 mm.
Among all these target positions, the points 1, 2 and 3 are a first triplet of aligned target positions mounted on a same breadboard as depicted Fig. 19 (at bottom left). During the experiment, this breadboard has been displaced to also compose the points 4, 5 and 6 (Triplet 2), then the points 7, 8 and 9 (Triplet 3). If the developed coordinate multilateration

measurement system works properly, the relative distances between the different positions of this triplet should be the same at the different locations. Points numbered from 10 to 16 are isolated points depicted in black in Fig. 18.

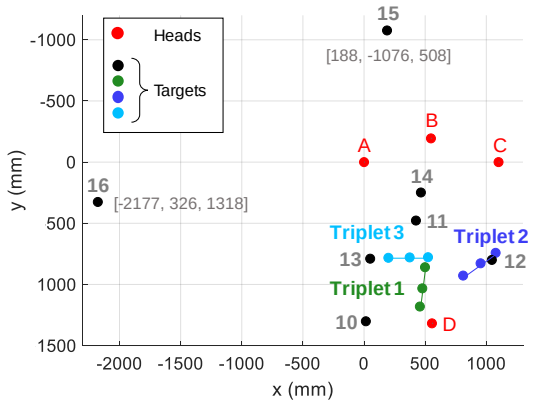

Fig. 18. Top view of the layout of the 4 measurement heads and 16 target positions.

The experiment was carried out in an air-conditioned room with a temperature around 19.9 °C, a pressure around 1010.80 hPa, and a humidity around 47.8%. From these values, each distance measurement has been corrected by the air group refractive index.

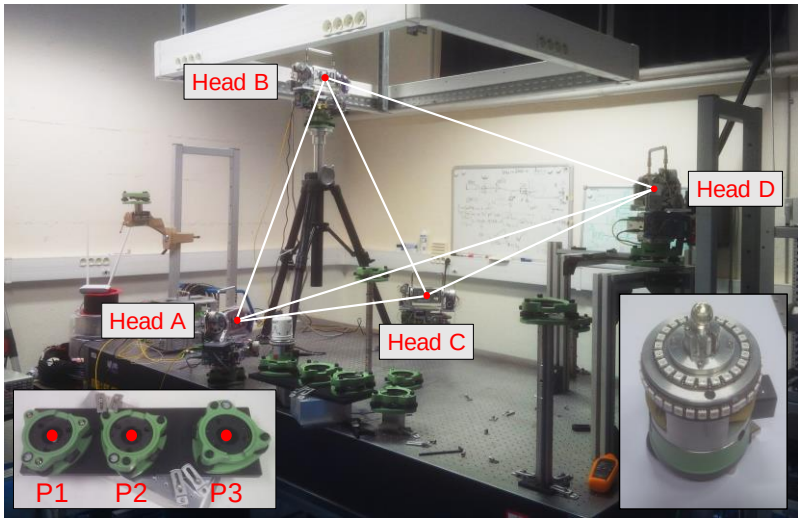

Fig. 19. Photograph of the experimental setup, with the triplet of aligned target positions on the bottom left, and the glass sphere n=2 mounted on a Leica carrier on the bottom right.

In practice, each target position is defined by a Leica tribrach, i.e. an adapter able to receive the target mounted on a Leica carrier. Thus, the target can easily be set by an operator at a given position. The four optical distance measurements are then performed after alignment of the measurement heads, one after another. Then the target is moved to the next position to obtain at the end a set of 64 measurements, 16 per measurement head. Each of these distance measurements is an average value over 576 points recorded over 20 s, a point corresponding to 20 ms integration time.

6.2. Data processing

The multilateration algorithm with self-calibration requires accurate initial values in order to converge efficiently. Since the measurement heads are equipped with angle encoders of around 400 µrad of resolution, the initial values of the target positions are determined from measurements of distances and angles of one of the four measurement heads, in the same way as a laser tracker. Thus, in a cartesian system, the 16 initial positions of the target j are:

$$x_j = d_{i,j} \times \sin(\varphi_{ij}) \times \cos(\theta_{ij}), \quad y_j = d_{i,j} \times \sin(\varphi_{ij}) \times \sin(\theta_{ij}), \quad z_j = d_{i,j} \times \cos(\varphi_{ij}) \qquad (12)$$

with $d_{i,j}$ the measured distances, θ_{ij} and φ_{ij} the azimuth and elevation angles of the measurement head i when it aims at the target j. Once the 16 initial target positions are determined, the initial coordinates of the four measurement heads are calculated by a classical multilateration algorithm [28].
Fig. 20 depicts the difference between the distances measured by the telemetric system and the distances obtained from the coordinates of the measurement heads and of the targets. For each target position, four errors are thus calculated, one

per head. The global standard deviation is equal to 0.80 mm. This gives an order of magnitude of the uncertainties of the coordinates of the measurement heads used as initial values into the self-calibration algorithm.

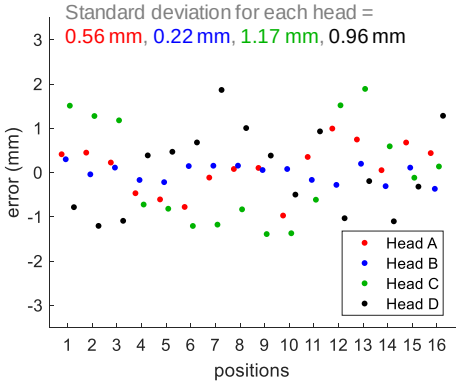

Fig. 20. Differences between the measured distances and the distances obtained by three-dimensional coordinate differences using the polar measurements based on distances and angles.

To determine the 16 positions T_j of the target and the 4 positions H_i of the measurement heads using length measurements only, a multilateration algorithm with self-calibration based on [14] has been developed. It consists in a nonlinear optimization problem where the quadratic sum of the differences between the squared distances measured by our ADM, $d_{i,j}^2$, and the squared distances calculated from the positions provided by algorithm is minimized:

$$\text{cost function} = \Sigma \left((d_{i,j} - o_i)^2 - \| H_i - T_j \|^2 \right)^2 \qquad (13)$$

The unknown variables to determine are, of course, the coordinates of the 16 target positions and of the 4 measurement heads, but also the instrument offset of each measurement head, named o_i. The latter is an additive constant that compensates from delays in electrical cables and optical paths. Thanks to these corrections, absolute distance measurements can be achieved between each measurement head and the target.
To minimize the cost function described in formula (13) correctly, at least ten target positions have to be measured [14]. This is the minimum of points required to have an equation system with more observations than unknowns. In our experiments, with 16 points, this condition is largely satisfied: this redundancy helps the algorithm to converge.

6.3. Experimental results

Fig. 21 presents the results after applying the multilateration algorithm with self-calibration. In this figure, the error is the difference between the distances measured by the telemetric system and the distances deduced from the multilateration algorithm that provides the coordinates of the measurement heads and of the targets. For each target position, four errors are still calculated, one per head. With errors lower than 12 µm and a standard deviation around 3.3 µm, it can be concluded that the multilateration algorithm with self-calibration has perfectly converged.

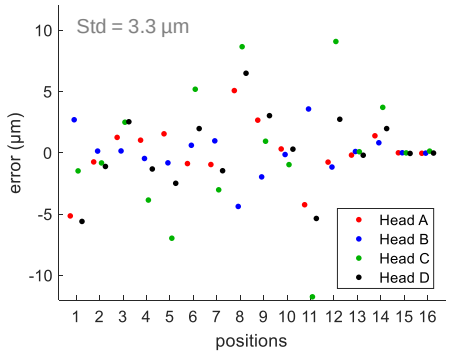

Fig. 21. Experimental results of the multilateration with self-calibration.

In parallel, the relative distances between the different positions of the triplet have been measured in a direct way by the ADM; it means without multilateration. To this end, the measurement head A has been positioned in the alignment of the three positions of the triplet, then by moving the target from one position to another, the relative distances between them can be determined:

$$\| \text{P1-P2} \|_{ref} = 150.096 \text{ mm} \pm 5.3 \text{ µm}, \| \text{P2-P3} \|_{ref} = 174.410 \text{ mm} \pm 2.2 \text{ µm},$$
$$\text{and } \| \text{P1-P3} \|_{ref} = 324.506 \text{ mm} \pm 1.9 \text{ µm}.$$

The uncertainties on the relative distances correspond to the standard deviation over 9 successive measurements. These uncertainties include the performances of the ADM and the centering repeatability of each tribrach, i.e. when the target

is removed and mounted again in the tribrachs with unchanged levelling and orientation of the carrier. According to [29], centering repeatability is between 2 and 5 µm.

Table III. Comparison of the triplet distances: direct distance measurements versus multilateration results.

Triplet	$\| P1\text{-}P2 \| - \| P1\text{-}P2 \|_{ref}$	$\| P2\text{-}P3 \| - \| P2\text{-}P3 \|_{ref}$	$\| P1\text{-}P3 \| - \| P1\text{-}P3 \|_{ref}$
1	-5.0 µm	0.8 µm	-5.9 µm
2	-7.8 µm	12.0 µm	2.5 µm
3	10.4 µm	11.9 µm	20.6 µm

The distance differences for the different positions of the triplet are below 21 µm, with standard deviation on these differences of 9.8 µm. This is a little bit higher than the combined standard uncertainty between the reference distances (between 1.9 µm and 5.3 µm at k=1) and the distances measured by our multilateration system (4.3 µm at k=1 since for short distances the SCR is higher than 60 dB). The multilateration algorithm with self-calibration adds therefore uncertainties to the measured positions, which will be quantified through a future study.

7. Conclusion

We have developed a multilateration system composed of a common ADM and of four measurement heads. It has been validated using a glass sphere of refractive index n=2 as retroreflector instead of a hollow corner cube. In this case, the range of our system is limited since at least 18 dB more optical losses are induced by the bad reflectivity of this target and the beam deflection at its output.

Nevertheless, it has been demonstrated that it is possible to optimize the received power for distances up to 20 m by slightly adjusting the focal length of the parabolic mirror used for beam collimation. By this way, the laser beam at the output of a measurement head converges up to 10 m before diverging. The received power is thus sufficient up to 20 m since the SCR is higher than 50 dB and the contribution of the crosstalk to the uncertainty on a distance measurement is reduced to 11.2 µm (k=1). In practice, only one head has been adjusted to have such an optimal beam configuration. The other measurement heads, with a beam collimation complying with the value of the focal length of the parabolic mirror, can claim similar performances for distances up to ~10 m only.

The uncertainty budget of the whole system has been established, and the uncertainties concerning the ADM has been experimentally validated thanks to a comparison with an interferometric bench up to 38 m. At the end, it has been shown that the uncertainty on a distance measurement using a glass sphere as a target is mainly limited by the SCR. However, with a SCR higher than 60 dB, the standard deviation of the difference between the interferometric measurements and the ADM ones was 3.3 µm, for an expected value of 4.0 µm at 60 dB of SCR.

In parallel, it has been verified that the in-house fastening system we have developed to maintain the glass sphere, a harness with three arms of 0.30 mm wide, does not perturb the distance measurements. It appears that the received power can vary when the incident beam crosses one of the arms, but the measured distance is not affected as long as the SCR remains at an acceptable level.

Lastly, the performances of the developed system have been validated through position measurements based on a multilateration technique with self-calibration. This was performed over a small volume with distances up to 3.5 m: the three-dimensional coordinates of 16 target positions have been determined, the multilateration algorithm with self-calibration has perfectly converged, and the position errors have been estimated at 21 µm in the worst case with a standard deviation around 10 µm.

In the future, the developed system will be improved for multilateration measurements over larger volumes. To this end, the measurement heads should be modified, more specifically their beam collimation, to optimize the signal propagation up to 20 m. This can be an opportunity to simplify the collimation system, currently based on a parabolic mirror, for a multi-element lens design for the collimation paired with a deflection mirror mounted on piezoceramic actuators for the aiming of the target.

Acknowledgment

This work was partially funded by Joint Research Projects (JRPs) 17IND03 LaVA and 18SIB01 GeoMetre, projects that have received funding from the European Metrology Programme for Innovation and Research (EMPIR) co-financed by the Participating States and from the European Union's Horizon 2020 research and innovation programme.

The authors are very grateful to Andrew Lewis, Ben Hughes and Michael Campbell from National Physical Laboratory (NPL, UK) for sharing glass spheres of refractive index n=2 for first tests, and to J. Cali and S. Durand from École Supérieure des Géomètres et Topographes (ESGT, FR) for the availability of their interferometric bench.

Reference

[1] Z. Wang, R. Zhang and P. Keogh, "Real-Time Laser Tracker Compensation of Robotic Drilling and Machining", Journal of Manufacturing and Materials Processing, vol. 4, issue 3, 79, 2020.

[2] C. Moeller, H.C. Schmidt, P. Koch, C. Boehlmann, S. Kothe, J. Wollnack and W. Hintze, “Real Time Pose Control of an Industrial Robotic System for Machining of Large Scale Components in Aerospace Industry Using Laser Tracker System”, SAE International Journal of Aerospace, vol. 10, issue 2, 2017.
[3] O. C. Martin, Z. Wang, P. Helgosson, J. E. Muelaner, A. Kayani, D. Tomlinson and P. G. Maropoulos, “Metrology enhanced tooling for aerospace (META): A live fixturing, wing box assembly case study”, 7th International Conference on Digital Enterprise Technology (DET), Athens, Greece, 2011.
[4] R. J. Leão, C. R. Baldo, M. L. C. C. Reis and J. L. A. Trabanco, “Engineering survey planning for the alignment of a particle accelerator: part I. Proposition of an assessment method”, Measurement Science and Technology, Volume 29, Number 3, 034006, 2018.
[5] Y. Gu, C. Liu, J. Wei, K. Lu, H. Ji, Y. Zheng, X. Fan, J. Wang, Z. Yuan and Z. Gong, “Study on the dimensional metrology and alignment method for the 1/32 CFETR VV mock-up”, Fusion Engineering and Design, vol. 155, p. 111556, 2020.
[6] A. Leon-Huerta, M. Lucero Alvarez, E. Hernandez Rios, C. Tzile Torres, L. Cabrera Cuevas, D. Castro Santos, J. Hernandez Lázaro, D.M. Gale, G. Wilson and G. Narayanan, “Alignment of a large outdoor antenna surface using a laser tracker”, SPIE Optical Metrology Conference, Munich, Germany, May 2013.
[7] M. Lösler, R. Haas, C. Eschelbach and A. Greiwe, “Gravitational deformation of ring-focus antennas for VGOS: first investigations at the Onsala twin telescopes project”, Journal of Geodesy, Volume 93, Issue 10, pp. 2069-2087, 2019.
[8] M. Lösler, C. Eschelbach, S. Riepl and T. Schüler, “A Modified Approach for Process-Integrated Reference Point Determination”, Proceedings of the 24th European VLBI Group for Geodesy and Astrometry Working Meeting, Las Palmas de Gran Canaria, Spain, December 2019.
[9] API Radian Pro, 2018. Available on: https://apimetrology.com/wp-content/uploads/2018/09/2018-API-Radian-3D-Laser-Tracker-Systems-Brochure.pdf. Accessed date: 25 june 2020.
[10] B. Muralikrishnan, S. Phillips and D. Sawyer, “Laser trackers for large-scale dimensional metrology: A review”. Precision Engineering, vol. 44, pp. 13-28, 2016.
[11] J. E. Muelaner, Z. Wang, O. Martin, J. Jamshidi and P.G. Maropoulos, “Verification of the indoor GPS system, by comparison with calibrated coordinates and by angular reference”, Journal of Intelligent Manufacturing, Volume 23, Issue 6, pp. 2323-2331, 2012.
[12] P. Pérez Muñoz, J. A. Albajez García and J. Santolaria Mazo, “Analysis of the initial thermal stabilization and air turbulences effects on Laser Tracker measurements”, Journal of Manufacturing Systems, Volume 41, pp. 277-286, 2016.
[13] S. Robson, L. MacDonald, S. Kyle, J. Boehm and M. R. Shortis, “Optimized multi-camera systems for dimensional control in factory environments”, Proceedings of the Institution of Mechanical Engineers, Part B: Journal of Engineering Manufacture, Volume 232, Issue 10, 2016.
[14] D. Zhang, S. Rolt and P.G. Maropoulos, “Modelling and optimization of novel laser multilateration schemes for high-precision applications”, Measurement Science and Technology, Vol. 16, No. 12, pp. 2541-2547, 2005.
[15] J. Guillory, D. Truong and J-P. Wallerand, “Uncertainty assessment of a prototype of multilateration coordinate measurement system”. Precision Engineering, vol. 66, pp. 496-506, 2020.
[16] Hexagon website, product page of the super cat-eye reflector. Available on: https://www.hexagonmi.com/products/laser-tracker-systems/accessories-for-laser-tracker-systems/super-cateye-reflector. Accessed date: 18 august 2021.
[17] T. Takatsuji, M. Goto, S. Osawa, R. Yin and T. Kurosawa, “Whole-viewing-angle cat’s-eye retroreflector as a target of laser trackers”, Measure Science and Technology, vol. 10, number 7, 1999.
[18] S. Masuda, H. Nakajima, A. Winarno, T. Takamura, H. Matsumoto, S. Takahashi and K. Takamasu, "Novel design of ball-lens-based laser tracker using pulsed interferometer", Measurement Science and Technology, vol. 30, number 8, 085005, 2019.
[19] B. Hughes, M. A. Campbell, A. J. Lewis, G. M. Lazzarini, and N. Kay, “Development of a high-accuracy multi-sensor, multi-target coordinate metrology system using frequency scanning interferometry and multilateration”. Proceedings of SPIE, Videometrics, Range Imaging, and Applications XIV. 2017.
[20] Hoya glass datasheet, 2017. Available on: http://www.hoya-opticalworld.com/common/xls/HOYA20180401.xlsx. Accessed date: 24 august 2020.
[21] B. Yang and H. Friedsam, “Ray-tracing studies for a whole-viewing-angle retroreflector”, International Workshop on Accelerator Alignment, Grenoble, France, 1999.
[22] A. Egidi, A. Balsamo and M. Pisani, “High-Index Glass Ball Retroreflectors for Measuring Lateral Positions”, Sensors, Vol. 19, Issue 5, 1082, 2019.
[23] S. A. Self, “Focusing of Spherical Gaussian Beams”, Applied Optics, vol. 22, number 5, 1983.
[24] J. Guillory, M. Teyssendier de la Serve, D. Truong, C. Alexandre and J.-P. Wallerand, “Uncertainty assessment of optical distance measurements at micrometer level accuracy for long-range applications”, IEEE Transactions on Instrumentation and Measurement, Vol. 68, Issue 6, pp. 2260-2267, 2019.
[25] B. Muralikrishnan, D. Sawyer, C. Blackburn, S. Phillips, B. Borchardt and W.T. Estler, “ASME B89.4.19 Performance Evaluation Tests and Geometric Misalignments in Laser Trackers”, Journal of Research of the National Institute of Standards and Technology, vol. 114, number 1, pp. 21-35, 2009.
[26] J. Guillory, D. Truong and J-P. Wallerand, “Assessment of the mechanical errors of a prototype of an optical multilateration system”, Review of Scientific Instruments, vol. 91, issue 2, 025004, 2020.
[27] T. Takatsuji, Y. Koseki, M. Goto and T. Kurosawa, “Restriction on the arrangement of laser trackers in laser trilateration”, Measurement Science and Technology, vol. 9, number 8, pp. 1357-1359, 1998.
[28] A. Norrdine, “An Algebraic Solution to the Multilateration Problem”, International Conference on Indoor Positioning and Indoor Navigation, Sydney, Australia, 2012.
[29] J. Braun, M. Štroner, R. Urban and F. Dvoček, “Suppression of systematic errors of electronic distance meters for measurement of short distances”. Sensors, Volume 15, Issue 8, pp. 19264-19301, 2015.

Figure captions

Fig. 1. Functional diagram of the multilateration system.
Fig. 2. The second stage of the gimbal mechanism.

Fig. 3. The retroreflecting sphere and its in-house fastening system. On the left, a photograph of the developed target, and on the right, the 3D model with the feet of the holder in red.
Fig. 4. Propagation of the laser beam up to the target using ray tracing.
Fig. 5. Deflection angles at the output, i.e. after reflection, of a sphere of diameter 14.2 mm obtained from ray-tracing simulations.
Fig. 6. Received RF power as a function of the distance for different beam shapes. The horizontal lines show the RF power level for which the Signal to Crosstalk Ratio (SCR) takes different values for a crosstalk at -69 dBm.
Fig. 7. The intensities of a laser beam along the two main axes of the parabolic mirror and the 2D reconstruction of the beam profile.
Fig. 8. Beam diameters at $1/e^2$ as a function of the absolute distance from the measurement heads. On the left: beam diameters of the head C on both axes X and Y. On the right: equivalent beam diameters for the four measurement heads and for different positions of their piezoceramic actuators.
Fig. 9. Focal error and output waist as a function of the output waist location for the two axes, X is depicted with dots while Y is depicted with crosses.
Fig. 10. Impact of the harness: received power when the sphere is rotated around its vertical axis (at the top) and its horizontal axis (at the bottom).
Fig. 11. Photograph of the harness when one of its arm passes in front of the incident beam on the left and the corresponding RF power variations observed and simulated on the right.
Fig. 12. Impact of the harness when one of its arm passes in front of the incident beam coming from the left: effective reflection area in brown, and parts of the incident and reflected beam masked by the arm in red and blue, respectively.
Fig. 13. Comparison between an interferometer and the ADM using a corner cube as target.
Fig. 14. Difference between the interferometer and the ADM with a corner cube as target.
Fig. 15. Comparison between an interferometer and the ADM using a sphere of n=2 as target.
Fig. 16. Difference between the interferometer and the ADM with the glass sphere as target and when the measurement head D is used.
Fig. 17. Difference between the interferometer and the ADM for small displacements.
Fig. 18. Top view of the layout of the 4 measurement heads and 16 target positions.
Fig. 19. Photograph of the experimental setup, with the triplet of aligned target positions on the bottom left, and the glass sphere n=2 mounted on a Leica carrier on the bottom right.
Fig. 20. Differences between the measured distances and the distances obtained by three-dimensional coordinate differences using the polar measurements based on distances and angles.
Fig. 21. Experimental results of the multilateration with self-calibration.

Table captions

Table I. Sources of errors of the telemetric system and their contributions when a glass sphere is used.
Table II. Analysis of the crosstalk.
Table III. Comparison of the triplet distances: direct distance measurements versus multilateration results.